Earth and Space Science

Key Points:
- Classification and height estimation of energetic intracloud lightning are investigated using RELAMPAGO Low-Frequency (LF) lightning waveforms
- A small number of high-peak current events and saturation of LF receivers hinder the observation of Energetic In-Cloud Pulses in RELAMPAGO
- A catalog of RELAMPAGO Compact Intracloud Discharges is produced to be used in future study of their occurrence in different storm types

Correspondence to:
A. L. Antunes de Sá,
andre.antunesdesa@colorado.edu

Energetic Intracloud Lightning in the RELAMPAGO Field Campaign

A. L. Antunes de Sá[1] [ID], **R. Marshall[1]** [ID], **and W. Deierling[1,2]** [ID]

[1]Smead Aerospace Engineering Sciences Department, University of Colorado Boulder, Boulder, CO, USA, [2]National Center for Atmospheric Research, Boulder, CO, USA

Abstract A particular strength of lightning remote sensing is the variety of lightning types observed, each with a unique occurrence context and characteristically different emission. Distinct energetic intracloud (EIC) lightning discharges—compact intracloud lightning discharges (CIDs) and energetic intracloud pulses (EIPs)—produce intense RF radiation, suggesting large currents inside the cloud, and they also have different production mechanisms and occurrence contexts. A Low-Frequency (LF) lightning remote sensing instrument array was deployed during the RELAMPAGO field campaign in west central Argentina, designed to investigate convective storms that produce high-impact weather. LF data from the campaign can provide a valuable data set for researching the lightning context of EICs in a variety of subtropical convective storms. This paper describes the production of an LF-CID data set in RELAMPAGO and includes a preliminary analysis of CID prevalence. Geolocated lightning events and their corresponding observed waveforms from the RELAMPAGO LF data set are used in the classification of EICs. Height estimates based on skywave reflections are computed, where prefit residual data editing is used to improve robustness against outliers. Even if EIPs occurred within the network, given the low number of very high-peak current events and receiver saturation, automatic classification of EIPs may not be feasible using this data. The classification of CIDs, on the other hand, is straightforward and their properties, for both positive and negative polarity, are investigated. A few RELAMPAGO case studies are also presented, where high variability of CID prevalence in ordinary storms and high-altitude positive CIDs, possibly in overshooting tops, are observed.

1. Introduction

Radiofrequency remote sensing of lightning provides crucial information in the research of thunderstorms and associated phenomena, where its significance lies in the variety of lightning types, often with a unique occurrence context and characteristically different electromagnetic emissions. Of these lightning types, cloud-to-ground (CG) lightning has been historically the most studied, because of a more direct impact on society and higher data availability, and it has been associated with high-energy emissions in the upper atmosphere above thunderstorms (Inan et al., 2010), such as sprites (Franz et al., 1990) and elves (Fukunishi et al., 1996; Inan et al., 1991). But interest on energetic intracloud (EIC) classes, that is, compact intracloud discharges and energetic in-cloud pulses, has been growing in the last couple of decades, accompanied by a greater understanding of the physical process behind them and their connection to other lightning-related phenomena, such as fast breakdown and Terrestrial Gamma-Ray Flashes (TGFs; Fishman et al., 1994).

Compact Intracloud Discharges (CIDs), also known as Narrow Bipolar Events (NBEs) or Narrow Bipolar Pulses (NBPs) based on their radio emission signatures, were first reported in the 1980s (Vine, 1980; Willett et al., 1989) and were remarked as strong emitters of HF-VHF radiation characterized by bipolar narrow electric field pulses (10–20 µs). The term CID was coined later by Smith et al. (1999), who associated the NBEs to other classes of intracloud discharges and inferred their relatively small spatial extent of hundreds of meters. CIDs were also found to occur either in isolation from other discharges in a storm or as the initiating event of an IC flash (Rison et al., 1999). Smith et al. (1999) also noted that the events were so different from other lightning phenomena, that a novel type of discharge mechanism seemed to be required to explain them, while Eack (2004) stated that even if the breakdown mechanism was the same, with streamers or lightning leaders, the CID impulsive nature and high-peak RF power made them distinct from conventional lightning.

Supervision: R. Marshall, W. Deierling
Validation: A. L. Antunes de Sá, R. Marshall, W. Deierling
Visualization: A. L. Antunes de Sá
Writing – original draft: A. L. Antunes de Sá
Writing – review & editing: A. L. Antunes de Sá, R. Marshall, W. Deierling

Even after four decades of study, there is still no consensus on the mechanisms responsible for CIDs, though that is quickly changing. A possible mechanism based on a relativistic runaway electron avalanche (RREA), seeded by an extensive atmospheric shower (EAS) of cosmic rays, was introduced by Gurevich et al. (2004) and Gurevich and Zybin (2005). Following the same RREA-EAS theory, Watson and Marshall (2007) used a modified transmission line model and an exponentially increasing current with altitude to show agreement with electric field change measurements of CIDs. Nag and Rakov (2010) then explained the radio signature of CIDs, particularly their secondary peaks, with a bouncing wave model, where the current oscillates between the two ends of the short channel associated with CIDs. In contrast, Arabshahi et al. (2014) showed that thunderstorm electric fields and cosmic ray energies required to match measured CIDs with the RREA-EAS model were not realistic. Finally, Rison et al. (2016) proposed that CIDs are caused by a type of fast positive breakdown, a precursor mechanism they suggest is associated with all ICs and possibly CG lightning flashes, which was supported by Liu et al. (2019); Tilles et al. (2019) additionally observed a type of fast negative breakdown producing CIDs as well.

Another distinct class of energetic ICs, Energetic In-cloud Pulses (EIPs), were identified by Lyu et al. (2015). As suggested by the bimodal distribution of the impulse charge moment change (iCMC) for high-peak current lightning (Cummer et al., 2013), there was already a strong indication that other high peak current IC events, besides CIDs, might be able to emit strong RF radiation. In contrast to CIDs, EIPs last an order of magnitude longer and are not isolated, spatially or temporally, but instead are associated with smaller discrete pulses within its associated time window, generally embedded in other electrical activity during a storm. Furthermore, in an analysis of a sample of CIDs and EIPs occurring over 44 days in the fall in the Southeastern USA, Lyu et al. (2015) inferred that negative CIDs occur at a higher altitude than positive EIPs. In that study, negative CIDs were observed at 16–19 km altitude, considered to be the strongest convection altitude during storms, between the upper positive and negative screening charge layers in a standard tripole storm. The positive EIPs were produced at 10–13 km within a weaker convection region between the main negative and upper positive charge layers. Both positive and negative EIPs have been associated with a different subset of Terrestrial Gamma-Ray Flashes (TGFs) (Lyu & Cummer, 2018; Lyu et al., 2015, 2016, 2018), the strongest source of natural radiation on Earth occurring above thunderstorms in the upper atmosphere; the EIP-TGF association indicates that they may be linked by the same production mechanism. A link between elves, EIPs, and TGFs has also been suggested (Liu et al., 2017).

The EIP production mechanism is associated with the propagation of negative leaders, upward leaders with +EIPs, and more rarely downward leaders with -EIPs, though it was originally not clear if EIPs were energetic leaders themselves. Recent radio interferometry observations provide clarification on the leader-EIP-TGF connection, and suggest that EIPs are generated by the relativistic discharge responsible for an accompanying TGF, rather than by streamer or leader activity (Tilles et al., 2020). The EIP production mechanism is thus markedly different from that of CIDs, as also indicated by the different temporal and spatial contexts in which they occur.

In this paper, EICs from different storms during the RELAMPAGO field campaign are investigated. The classification of EIC lightning types is described and validated, with supporting VHF and E-field change data available during the campaign. The prevalence of EICs and some of their properties during RELAMPAGO storms are discussed.

2. Background

2.1. RELAMPAGO Field Campaign

The Remote sensing of Electrification, Lightning, And Mesoscale/Microscale Processes with Adaptive Ground Observations (RELAMPAGO) field campaign was conducted from November to mid-December 2018, parts of the campaign started earlier in 2018 and extended through early 2019 in west central Argentina, in the vicinity of the Sierras de Córdoba and near the city of Mendoza at the foothills of the Andes mountains (see Figure 1). Primarily funded by the National Science Foundation, this campaign was an international collaboration seeking to observe and investigate convective storms that produce high-impact weather (Nesbitt, 2020). This region of Argentina is known to exhibit some of the most intense storms in the world as well as the highest lightning flash rate per storm system (Cecil et al., 2015; Zipser et al., 2006). An
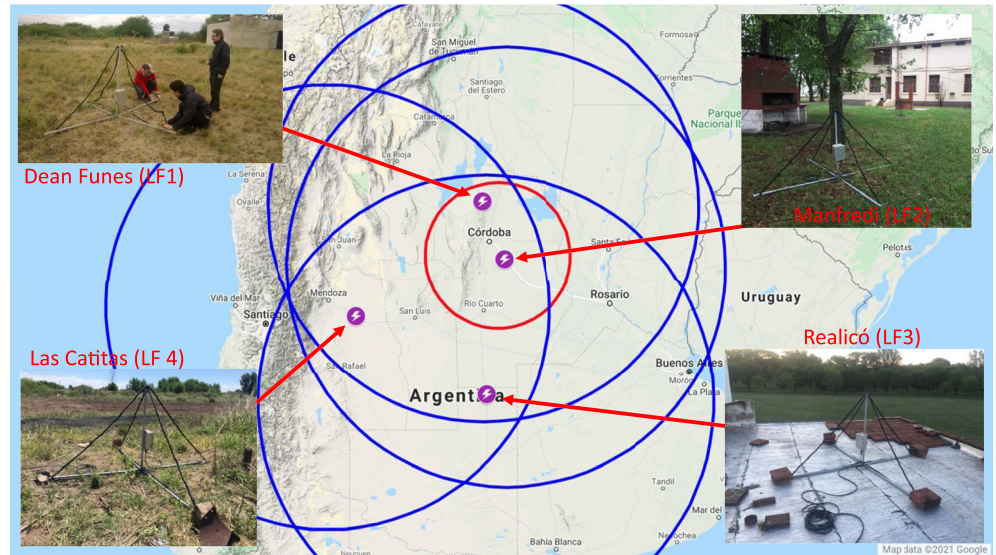
Figure 1. RELAMPAGO deployment map of the Low-Frequency (LF) instrument in Argentina, and a collection of photos taken during the deployment. The photos showcase the instrument's outdoor antenna structure, consisting of two orthogonal magnetic loop antennas. The blue circles indicate an approximate sensitivity range for the LF instruments (600 km), and the 150 -km red range circle defines the main region of interest in RELAMPAGO where the majority of other sensors were deployed.

association of severe weather with storms occurring in this region is supported by radiometer observations (Cecil & Blankenship, 2012) and public reports (Rasmussen et al., 2014).

The RELAMPAGO campaign incorporated a multitude of instrument types, particularly during the intensive observation period between November 1 and December 15, 2018. Lightning-observing instrumentation included an array of four Very Low Frequency/Low Frequency (VLF/LF) autonomous magnetic sensors (LFAMS or "LF instrument") deployed by the University of Colorado Boulder; a 11station Lightning Mapping Array (LMA; T. J. Lang et al., 2020) deployed by NASA's Marshall Space Flight Center, an array of eight electric field mills (EFMs; Antunes de Sá et al., 2020) deployed by the University of Colorado Boulder, and an array of 8 field change meters (CAMMA; Zhu et al., 2020) deployed by the University of Alabama Huntsville. Many other instruments were deployed or operating during the campaign, including radars, hail pads, and soundings; see Nesbitt (2020) for a full list of deployed instrumentation and an overview of the field campaign. This paper makes use of the geolocated lightning data from the LF instruments (Antunes de Sá et al., 2021), which were deployed to cover a large area including and between Mendoza and Cordoba (Figure 1). Other RELAMPAGO data sets are also used in this investigation on RELAMPAGO EICs, including the LMA (T. Lang, 2020) and CAMMA data sets (Carey et al., 2019a, 2019b; Zhu et al., 2020). Unaffiliated data sets that observed RELAMPAGO storms are also used, such as from NOAA's Geostationary Operational Environmental Satellite R series (GOES-R) Advance Baseline Imager (ABI; GOES-R Calibration Working Group & GOES-R Program Office, 2017) and Geostationary Lightning Mapper (GLM; GOES-R Series Program, 2019) instruments and from the Earth Networks Total Lightning Network (ENTLN; Heckman, 2014).

2.2. RELAMPAGO LF Data Products

A brief overview of the deployed LF system and LF data sets that are used in this study to identify various lightning types is provided below.

The LF instruments deployed in the RELAMPAGO campaign are based on the 100-kHz sampling rate VLF instrument described by Cohen, Inan, & Paschal (2010), with the proper modifications for operating at a 1-MHz sampling rate and collecting VLF/LF (3–400 kHz) data. The instrument's antenna element consists of two air-core magnetic loop antennas aligned with North-South (Channel 1) and East-West (Channel 2) direction. The instrument continuously records radio signals arriving at the antennas, referred to as the LF
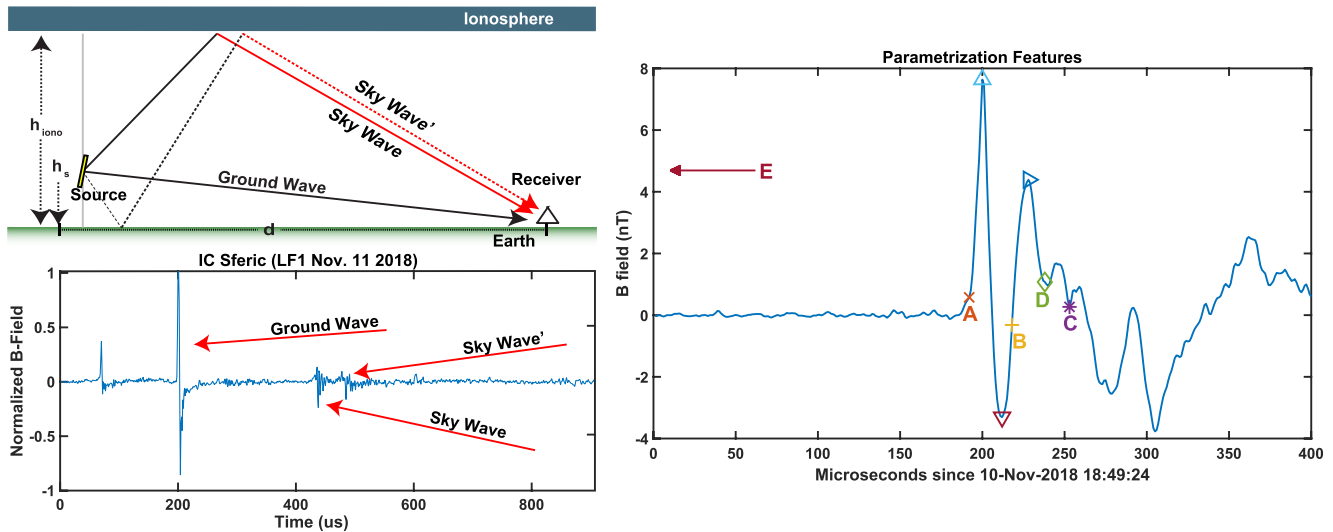
Figure 2. Illustrations of the lightning emission propagation path toward the receiver, using a simplified flat-earth assumption, adapted from Marshall et al. (2015) (top), an IC sferic received by LF1 during RELAMPAGO (bottom), and waveform features *A–E* used in the EIC parameterization suggested by Lyu et al. (2015) (right). The paths illustrated and identified in the sferic include a ground wave, propagated directly between source and observer, sky waves, and ionospheric reflections. The ground-ionospheric path is only observed for intracloud, where the source height is larger than zero. Paths with more hops are also possible but are rarely observed due to stronger attenuation.

Level 0 (raw) data set. Two data products have been released after hierarchical processing of the raw data. The Level 1 data set (Deierling et al., 2019) is a station-specific collection of lightning waveform data (radio atmospherics or sferics) extracted from the Level 0 data. The Level 2 data product (Deierling et al., 2021) provides information on geolocated lightning events (discharges) and lightning flashes from the Level 1 sferic observations. A detailed description of the instrument, RELAMPAGO deployment, data processing, and data products can be found in the accompanying documentation to the data products and in Antunes de Sá et al. (2021).

2.2.1. Level 1 Data Product

The processing for this data product mainly consists of a peak magnitude search for sferics across the raw data (quadrature addition of the two channels) with a peak stronger than five times the raw data noise floor. Once a possible sferic has been identified, a data window of 1.2 ms is extracted from both channels with the main peak centered at 200 μs. Power-line noise at 50 Hz and harmonics is removed from the data filtered using a "Humstractor" algorithm (Cohen, Said, & Inan, 2010). Figure 2 presents an illustration of the propagation paths from a typical lightning emission, an example Level 1 sferic from the LF1 receiver, and waveform features used in Section 3.1 for EIC classification. Saturated sferics were observed whenever a strong lightning radio emission induced a greater B-field at the antennas than the instrument could measure, and it was caused by a combination of large peak current lightning discharges and discharges in close proximity to the LF instrument. The main peak in the sferic can be clipped down to the instrument saturation level or attenuated if in the nonlinear regime of the receiver near saturation.

2.2.2. Level 2 Data Product

The Level 2 data processing, summarized in Figure 3, involves matching the Level 1 sferics, using cross correlations, into lightning events and extracting time-of-arrival observations for geolocation. Geolocation is then accomplished using a linearized least squares (LSQ) statistical filter, which assumes an unbiased Gaussian distribution of time of arrival uncertainty of 10 μs, a spherical time-of-arrival model, and negligible model and linearization errors. The time of arrival uncertainty is a best guess based on the station clock error correction performed at an earlier stage. To ensure the linearization assumption, a low-precision a priori is generated using the nonlinear time-of-arrival model and subsequently fed into the least squares filter. Peak current is estimated using peak magnitude observations of an event and an attenuation model based on finite-difference time-domain (FDTD) simulations of lightning propagation (Marshall, 2012), under the
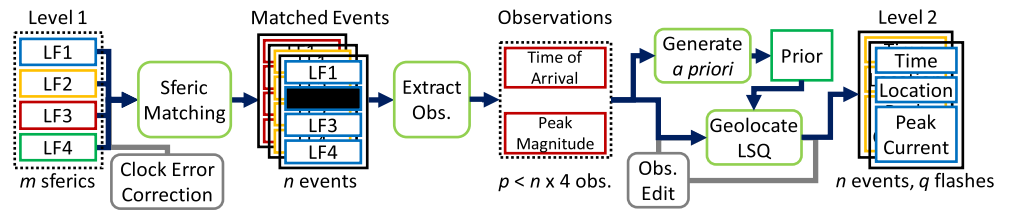
Figure 3. Flowchart describing the geolocation data processing for generating the Level 2 data product. The gray ad hoc processes are only necessary in handling specific issues with the RELAMPAGO data set.

assumption that a known peak-radiated field, a distance away from the source, for example, 100 km, is proportional to the source's peak current by a constant parameter (Orville, 1991). Peak current estimates are set to infinity for events that saturated all observing receivers. A domain mask is used to discard geolocated events outside the observable region of the LF array, which varies depending on which LF stations made an observation for a specific event. A quality measure is computed at the matching step for each event based on the minimum cross-correlation score across its sferics. Additionally, geolocated events are clustered into lightning flashes based on the spatiotemporal distance criteria of 10 km to the flash centroid and 0.3 s to the last event of a flash.

Flash geolocation accuracy was estimated to be better than 10 km, and a flash detection efficiency comparable to that of GLM was observed in the roughly 400-km LF deployment center region (Antunes de Sá et al., 2021). Detection efficiency losses due to station availability and sensitivity changes were also observed and investigated.

In order to capture the strongest high-peak current events, possibly not captured in the LF Level 2 data due to receiver saturation, ENTLN pulse data (analogous to LF Level 2 events) with reported peak currents higher than 100 kA are matched to RELAMPAGO LF Level 1 data and appended to the Level 2 data set specifically for this study. Note that this relaxes the Level 2 event requirement of having at least 3 sferic observations for an event, as one sferic is enough for an ENTLN-based event. A large number of ENTLN events are actually in the LF Level 2, some with underestimated LF Level 2 peak currents, some with similar peak currents, and most with LF Level 2 peak current set to infinity due to saturation. To avoid duplicating these events, the matching ENTLN pulse information replaces those LF Level 2 event entries. A match is considered when an ENTLN event is within 0.3 ms and 25 km of sferics used in an LF event entry, corrected for the propagation delay expected from the ENTLN-reported source location to our LF receivers. About half of the ENTLN events are seen in the LF data, with periods of higher LF loss such as November 10 and 11, and other times with more matches. Of all the lightning events classified in Sections 5 and 4, that is, LF events with peak currents higher than 10 kA, only a small percentage, <1%, are actually taken from ENTLN 100+ kA.

3. Event Processing

3.1. EIC Classification

Automatic classification of CID sferics was first demonstrated by Smith et al. (2002), leveraging the fast rise and fall times of the CID pulse and temporal isolation from other VLF/LF emissions from lightning processes. Smith et al. (2002) showed that in the two-parameter space of rise-plus-fall time and signal-to-noise ratio, the distinction between the CID and nonCID population was strong enough to allow for a criterion-based classification (see Figure 14, Smith et al., 2002). Similarly, following the discovery of EIPs, Lyu et al. (2015) proposed a CID/EIP classification scheme based on three time-domain parameters: pulse width (related to rise-plus-fall time), peak ratio (ratio between opposite polarity peaks in bipolar EIC pulses), and isolation ratio (related to signal-to-noise ratio). Lyu et al. (2015) manually identified CIDs and EIPs in 44 days of storms in the southern United States during the fall season, and also found a distinction between the lightning-type populations. Note that Lyu et al. also implicitly used peak current and CG-IC type as extra classification parameters, only classifying lightning events with a National Lightning Detection Network (NLDN) peak current estimate higher than 200 kA and categorized by NLDN as IC lightning.

The three-parameter classification suggested by Lyu et al. (2015) is adopted in this paper, with implementation details and changes described in this section. The RELAMPAGO LF geolocated events data (Level 2 data), which provide time, location, and peak current, in conjunction with the corresponding LF sferic observations for each event (Level 1 data) are used. The classification is directly applied to all of the LF data in RELAMPAGO, without peak current or CG-IC type constraints, and peak current is used as a fourth parameter in classification. The 200-kA requirement in Lyu et al. (2015) is restrictive in order to collect only "highly energetic" ICs, and they acknowledge that the NLDN peak current estimate, which is effectively a scaled and normalized peak radiated electric field also used in the RELAMPAGO LF data, is not a well-calibrated measurement for IC lightning.

The classification parameters are derived from key features of the observed sferic waveform, per Lyu et al. (2015) and illustrated in Figure 2: A preceding the initial peak and at 10% of its maximum value; B following the main peak and at 10% of its maximum; C following the overshoot peak and at 10% its maximum; D at 20 μs after B; and $E \sim 500$ μs preceding A. The parameters are then defined per Lyu et al. (2015) as follows: pulse width is the duration of the pulse, the time duration between A and C; the peak ratio is the ratio between the first peak in the sferic pulse (initial peak) and the second peak in the pulse (main peak), in the AB window; and isolation ratio is the sum of the preceding and post activity ratios. This activity ratio γ is defined in Equation 1 with the top sum over points in the window AB and the bottom sum over points in the window EA for preceding activity or over points in the window BD for post activity:

$$\gamma = 10 \times \log_{10} \left[\frac{\frac{1}{M} \left(\sum_{i=1}^{M} B_i^2 \right)}{\frac{1}{N} \left(\sum_{j=1}^{N} B_j^2 \right)} \right] \tag{1}$$

Our specific implementation of the waveform feature extraction relies on positive identification of the initial, main, and overshoot peaks, and includes basic quality control. The identification of the initial peak, which is the most important feature for successful EIC classification since all other features depend on it, actually starts in the Level 2 data processing. In the Level 1 data, the 1.2-ms extracted sferic has its highest peak centered at the 200th μs, but it often does not capture the initial peak of the sferic. For the identification of the initial peak only, the sferic is filtered by a lowpass IIR 12-order butterworth filter with a cutoff frequency at 10 kHz and the first peak in the window is selected to be the initial peak at the 200th μs, correctly capturing pulses with a weaker groundwave. A cross-correlation score is computed for different sferic observations of the same event, and bad matches, including those with poor alignment, are reflected in this score for later quality control. The applied shifts to the Level 1 data are reported in the Level 2 geolocation process. In the classification algorithm, with the applied shifts to the sferics, the initial and main peaks are found to be the minimum and maximum peaks, respectively, or vice versa for negative polarity pulses, in the 150–250 μs window of the sferic. Both bipolar and unipolar pulses are captured, by setting the first peak to be the initial peak but only if it is smaller (greater) than 10% of the second peak, which is always true for bipolar pulses and only true for unipolar pulses with the initial peak being greatest in magnitude. This also limits all unipolar pulses to a peak ratio of at most 10. Note that EICs are bipolar with possible overshoots. A and B are then picked to be the first point in time that satisfy the criteria in the previous paragraph, with B not exceeding 100 μs from the main peak. The overshoot peak is found to be the next opposite-polarity peak within 30 μs of B, and again C is picked in the 35 μs window after the overshoot peak. If the overshoot peak or C cannot be found, C is set to be the same as B. For any other feature that cannot be found to satisfy the criteria, the classification is discarded. Note that the window limits are all within what is expected of EIC waveforms, but it is biased against the slowest CG waveforms. Also note that E is set to the beginning of the sferic record, which is at most 200 μs before the initial peak, and the classification is discarded if E is less than 100 μs before A to avoid overestimation of the isolation ratio.

With the classification parameters computed for every sferic observed for each event (maximum of 4 sferics per event, from our 4 LF receivers), the parameter's averages are used in the EIC classification. Because receiver saturation affects the observations, especially for higher peak current events close to the stations, the observations from saturated sferics are not used in the parameter's averages. If all stations saturated, the parameter from LF4 was used, if available, due to that station's much higher saturation point. Other saturation-related issues include some underestimation of high-peak currents or the inability to compute peak

current for very strong events, which are reported in the LF Level 2 data with an "infinite" peak current. In the worst case, saturation can cause heavy distortion of the sferic waveform, preventing successful matching and geolocation. In order to mitigate any loss of detection efficiency for high-peak current events in the LF event data, ENTLN events with peak current higher than 100 kA and without a coinciding LF Level 2 event were added to the eligible pool of LF events to be classified (described in Section 2.2.2).

3.2. EIC Height

Given the geometry of the lightning emissions, ground, and reflected skywaves (Figure 1), it is possible to estimate the lightning source height for ICs. Although the reflection mechanism at the ionosphere is more complicated than a perfect reflection, the assumption is acceptable within the uncertainties discussed here. Smith et al. (1999) derived a flat-Earth model of the skywave reflection geometry with the 1-hop ground-skywave delays, Δt for source-ionosphere and $\Delta t'$ for source-ground-ionosphere, given by

$$
\begin{aligned}
\Delta t c &= \sqrt{d^2 + (2h_{\text{iono}} - h_{\text{s}})^2} - \sqrt{d^2 + h_{\text{s}}^2} \\
\Delta t' c &= \sqrt{d^2 + (2h_{\text{iono}} + h_{\text{s}})^2} - \sqrt{d^2 + h_{\text{s}}^2},
\end{aligned}
\tag{2}
$$

where d is the great-circle distance between source and receiver, h_{iono} is the ionosphere reflection height, h_{s} is the source height, and c is the speed of light. This model is simple yet useful and has been used in CID height estimates (e.g., Wu et al., 2011, 2012), though a slightly more complicated spherical Earth method has also been used extensively (e.g., Smith et al., 2004; Zhang et al., 2016). The flat-Earth assumption produces a model error below 300 m for the source height estimate, which is much smaller than the uncertainty caused by the location precision of a few kilometers.

The skywave delay observations are extracted from the sferic records by finding the two strongest positive and two strongest negative peaks after the waveform feature D. The first of four peaks is checked to be followed by the opposite polarity peak within $20\,\mu s$. The groundwave initial or main peak is then subtracted from the skywave peaks, according to the order in which they appear in the sferic, that is, the first peak of a skywave is subtracted by the initial peak and the second peak of skywave, if it exists, is subtracted by the main peak. At best, each sferic yields four observations, if none are discarded throughout the process.

The source height and ionosphere height can then be estimated using the observations, which form an overdetermined system when more than two observations are acquired. A statistical linear least squares is employed in estimating the heights, with an assumed normal observation uncertainty of $2\,\mu s$ for each delay, estimated empirically from the observation detection and timing errors. Note that the uncertainty in the observation pairs from the same sferic is not independent, and violating that assumption leads to slight underestimation of height uncertainty. An a priori is given to the filter with a source height of 10 km and an ionosphere height between 88 km (night) and 73 km (day), with a fast transition during twilight, based on ionosphere height estimates in Smith et al. (2004) (Figure 6) and the RELAMPAGO data set. Since there is a large contribution of erroneously detected skywaves, which provide inaccurate height estimates, and the ionospheric height can be reasonably constrained, a data editing scheme is employed based on the filter innovation, that is, the prefit residual (observation-minus-expected). The mean innovation is computed for a reflection pair, minimizing the source height dependence, and if it is larger than 7.5 times the observation uncertainty of $2\,\mu s$ (or $15\,\mu s$, roughly equivalent to ± 4.5 km), that observation pair is discarded. Observation pairs that, by themselves, yield IC heights less than 5 km or higher than 24 km are also discarded.

The innovation filter is highly successful in removing bad observations, which could otherwise greatly affect the height estimate, since the filter is not robust to bad observations. Observations from all stations are weighted the same even though at least one station is likely to yield bad observations, for example, depending on lightning location and the fact that one pair of observations in a sferic is smaller and sometimes unidentifiable. Instead of removing stations, and only keeping the stronger reflection pair, the filter is able to utilize those observations when possible and increase estimate precision. For validation, a plot of ionosphere height estimates from EICs during November 12, 2018, is shown in Figure 4, where the method not only estimates a reasonable diurnal variation in the ionosphere height, but also discards outliers and
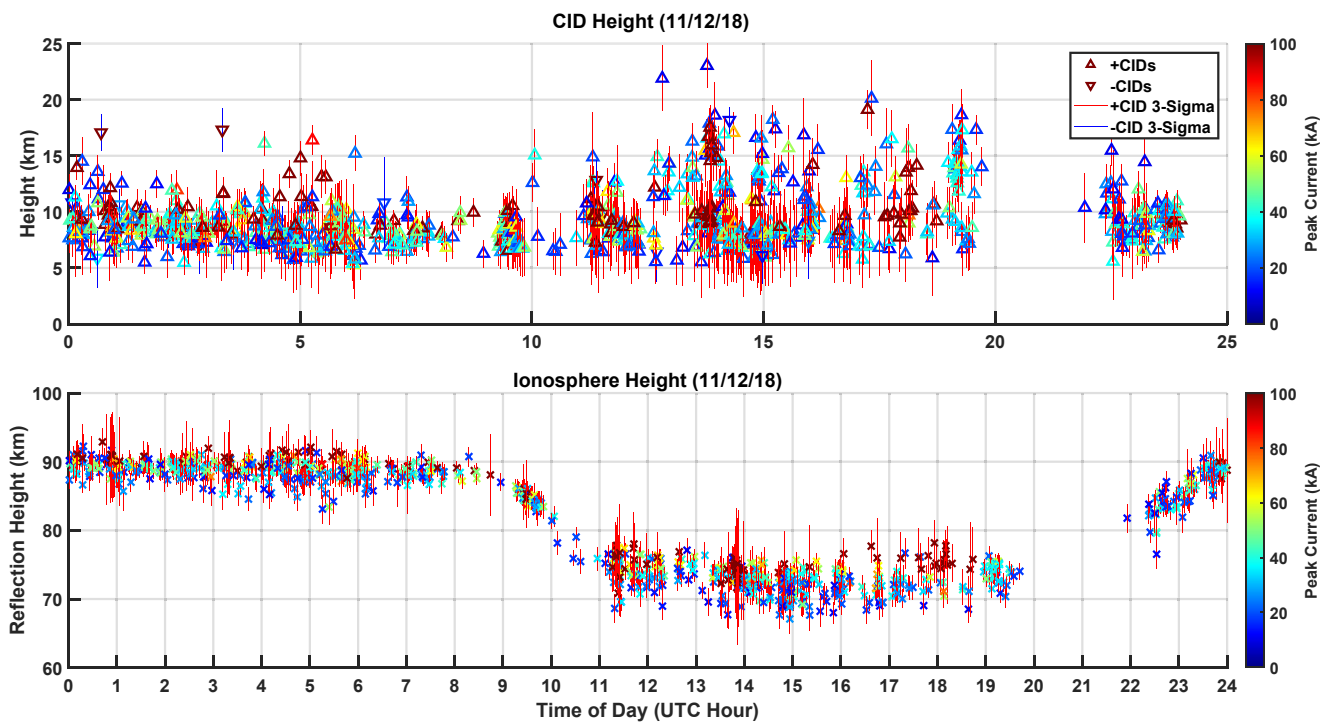
Figure 4. Plot of the Compact Intracloud Discharge (CID) and ionosphere height estimate that accompanies the height estimate of 1,075 CIDs, of which a height estimate could be achieved for 947 CIDs, during RELAMPAGO storms on November 12, 2018.

automatically selects the best observations to match the ionosphere height prior. Note that the innovation filtering has no direct impact on the source height estimate, except for the benefits of selecting the best observations for its computations, and is allowed to vary significantly from its prior of 10 km according to the observation model (Equation 2).

4. RELAMPAGO EICs

Classified EICs from the RELAMPAGO campaign are presented in this section and the classification results are investigated. There are about 100,000 lightning events collected by the LF system from select days during the RELAMPAGO campaign that were used in the classification. They are described in Table 1. Only events with an estimated peak current higher than 10 kA are classified, because the sferics associated with weaker events and lower signal-to-noise ratio start to lose waveform features to the noise floor. To give context to the events, flash information for the same period is also presented, including flash rates, average flash peak current, I_{pk}, average multiplicity, and the position in time of the highest peak current event in a flash, τ_{flash}, as a percentage. Flash peak current is reported as the maximum peak current of its constituent events, and τ_{flash} is only computed for flashes with multiplicity higher than one.

Figure 5 (top) shows the distribution of events on November 12, with the second highest number of events reported and highest average peak current in a single day, in the classification parameter space. As expected, the population of CIDs, with low pulse width and high isolation ratio, is distinct from the rest of the distribution. A selection criteria of pulse width less than 50 μs, isolation ratio higher than 60 dB, and no criterion for either peak current or peak ratio is chosen for CIDs. EIPs, on the

Table 1

RELAMPAGO LF Events, With Peak Current Higher 10 kA, Used in the EIC Classification and Their Average Peak Current, I_{pk}, are Presented to the Left for a Selection of Dates During the Campaign

Events ≥ 10 kA				Flashes				
Date	Count (#)	Rate (min⁻¹)	I_{pk} (kA)	Rate (min⁻¹)	Max rate (min⁻¹)	I_{pk} (kA)	Mult. (#)	τ_{flash} (%)
11/3/18	3,861	2.68	17.27	5.45	74	6.76	3.31	59
11/10/18	15,273	10.61	18.16	22.61	164	8.2	4.31	63
11/11/18	45,731	31.76	16.67	53.26	499	8.56	5.07	67
11/12/18	22,904	15.91	22.29	11.56	75	11.95	4.36	54
11/17/18	2,324	8.64	17.04	8.59	22	8.91	2.98	64
11/26/18	3,449	8.2	19.29	9.1	64	7.79	4.12	63
12/04/18	4,709	3.27	18.6	5.8	77	7.22	3.92	55
All	98,251	11.58	18.43	16.62	499	8.68	4.61	63

Note. All RELAMPAGO LF flashes are also presented for context, including average flash peak current, multiplicity, and the position in time of the highest peak current event in a flash, τ_{flash}, as a percentage.
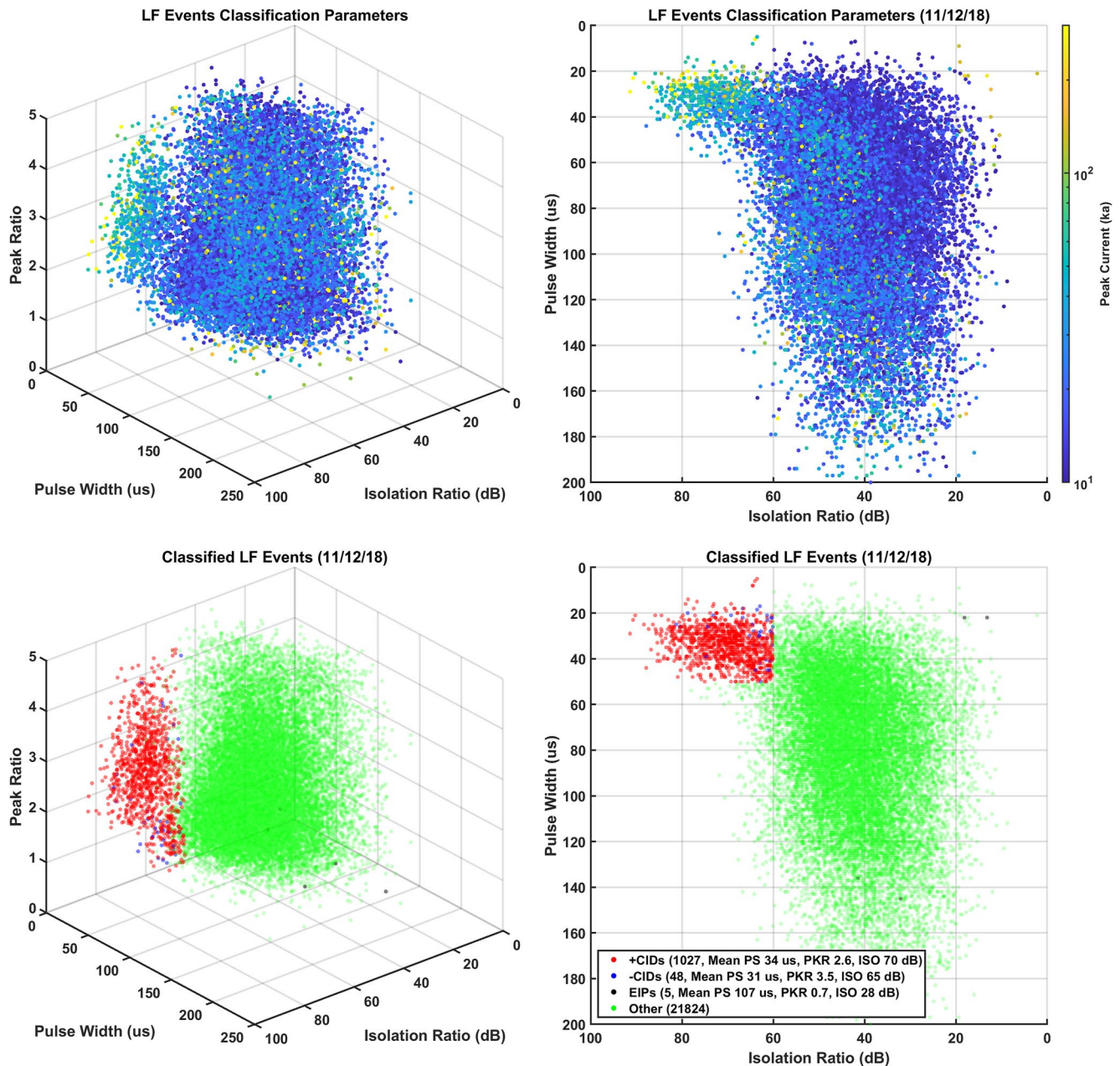
Figure 5. Distribution of RELAMPAGO Low-Frequency (LF) events in the classification parameter space (top), that is, pulse width (PS), peak ratio (PKR), isolation ratio (ISO), and peak current, and classified energetic intracloud LF events (bottom) on November 12, 2018, for the whole day on November 12, 2018. A low pulse-width high isolation population, expected for Compact Intracloud Discharges, is distinguishable from other events in agreement with Smith et al. (2002, Figure 14) and Lyu et al. (2015, Figure 1). The population of Energetic In-cloud Pulses, however, is not obvious.

other hand, are much harder to identify. Since only very high-peak current EIPs have been identified in the past, a peak current requirement is set for EIPs to record at least 200 kA of peak current, just as in Lyu et al. (2015). Also following the suggestions and discussions by Lyu et al. (2015), the EIP criterion for peak ratio is set to less than 1, that is, main peak stronger than initial peak. Other criteria were not set, given the already low number of potential EIPs, and so that more events could be investigated before being discarded.

The resulting EIC population after applying the selection criteria is shown in Figure 5 (bottom). Through manual validation of the sferic waveforms and against other RELAMPAGO data sets such as from the LMA or CAMMA, we find that the criteria for CIDs, used for all dates, successfully select the CID population.

Table 2
Properties of Classified Positive and Negative Polarity CIDs Classified From a Selection of Dates During the Campaign

Date	Count (#)	Count (%)	I_{pk} (kA)	h_s (km)	PS (μs)	PKR ()	ISO (dB)	Mult. (#)	τ_{flash} (%)
+CIDs									
11/3/18	0	0	N/A	N/A	N/A	N/A	N/A	N/A	N/A
11/10/18	570	3.73	26.62	13.73	21.8	2.43	66.79	2.65	54
11/11/18	458	1.0	43.6	9.66	34.4	2.28	67.42	3.82	0.36
11/12/18	1,027	4.48	44.27	9.31	34.07	2.58	70.47	3.55	24
11/17/18	63	2.71	19.45	9.07	35.22	1.62	63.75	2.78	55
11/26/18	97	2.81	24.7	8.83	35.25	2.07	69.34	4.82	39
12/04/18	78	1.66	17.16	9.82	37.51	1.31	63.74	4.82	41
All	2,293	3.38	37.32	10.47	31.28	2.39	68.48	3.46	36
−CIDs									
11/3/18	1	0.03	13.14	N/A	29.5	1.35	66.42	3	0
11/10/18	131	0.86	21.39	11.17	28.84	2.07	65.78	3.31	68
11/11/18	101	0.22	18.8	12.14	27.54	2.51	63.73	4.19	56
11/12/18	48	0.21	26.48	9.96	30.8	3.45	65.24	2.9	31
11/17/18	17	0.73	17.16	9.96	27.41	1.44	63.33	2.12	45
11/26/18	33	0.96	16.23	8.63	27.99	2.83	63.52	3.27	44
12/04/18	34	0.72	20.4	10.05	30.75	1.95	63.55	3.18	35
All	365	3.73	20.56	10.86	28.77	2.40	64.62	3.43	53

Note. These include a total count of CID, the percentage of CIDs in the pool of eligible events (Table 1), average peak current, average estimated source height (Section 3.2), average classification parameters pulse width (PS), peak ratio (PKR), isolation ratio (ISO), average multiplicity of its parent flash, and the average position in time of the CID within its parent flash, τ_{flash}, as a percentage.

Though the CID population slightly changes on different dates, with smaller pulse width average (faster), the 50 μs criterion captures the slower events of that population when they exist, and the 60 dB criterion prevents non−CID events from being captured when the population is faster. As these criteria are relaxed, the number of false-positive CIDs quickly increase and true-positive CIDs decrease. Some true positives still exist outside the selection region due to errors in the computation of classification parameter, for example, near-saturated/distorted sferics. With the chosen criteria, the number of false-positive CIDs is found to be small, <3%.

On the other hand, few potential EIP waveforms, if any, seem to agree with what is expected from past research (e.g., Liu et al., 2017; Lyu et al., 2015; Tilles et al., 2020). Most of the classified EIPs are actually highly saturated for all stations except LF4, and far enough away that the skywave blends with the groundwave main peak, artificially deflating the peak ratio measure to fulfill the EIP selection criteria. This is obvious from many potential EIP waveforms with similar features, and the corresponding CAMMA record for one of these EIP candidates coincides to within 1 ms and 5 km from two CAMMA sources near the ground, indicating a CG source. Additionally, the number of potential EIPs is very small, with just a handful occurring in well-observed RELAMPAGO storms and most at the edges of the LF observation region. Thus, this data set might not be able to provide further insights into EIPs, aside from their supposed absence in the LF observed RELAMPAGO storms and classification complexity under saturated and distant receivers. As such, we focus the present analysis on CIDs.

Table 2 presents the properties associated with the classified CIDs, including prevalence, average peak current, and source height. The most striking result is that the source height for +CIDs on November 10 is much higher than −CIDs. It is also accompanied by the smallest pulse widths recorded. The occurrence of the CIDs was associated with several supercell storms that occurred that day, two of which are investigated in Section 5. November 12, characterized by a very large number of discrete nonsevere storms, also
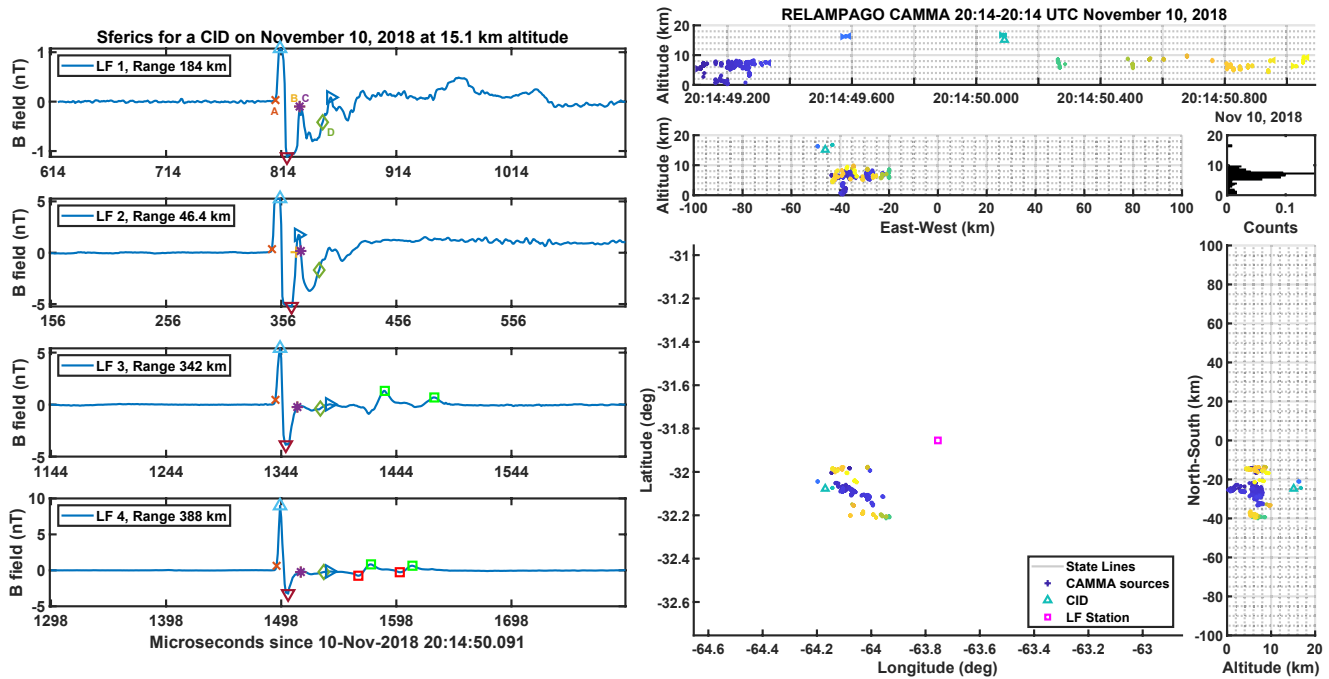
Figure 6. Panel of the Low-Frequency sferics observed for a +Compact Intracloud Discharge (left) and XLMA-style plot of CAMMA sources (right). Sferic features *A–D*, initial, main, and overshoot peaks, as well as skywave peaks (green and red squares) are displayed. On the right, CAMMA sources are color coded by time, and flash boundaries are depicted using right- and left-pointing triangles in the top plot.

displayed a large percentage of CIDs per storm, with one of these investigated in Section 5. Across all days, the source height distribution indicates higher altitudes for the rarer −CIDs than for +CID, as expected from past research, but not statistically significant given their uncertainties. A better understanding on the charge structure of the storms occurring on the investigated days is necessary for further conclusions about CID heights, some of which is provided in Section 5. The absence of CIDs on November 3 also needs to be investigated further for the individual storms on that day (not included in this study), given the similar count of LF events to November 17, 26, and December 4, which saw a much higher prevalence of CIDs. Finally, the distribution of τ_{flash}, the position in time of the CID within its parent flash, shows enough variability to prevent strong conclusions. Overall, in our study, +CIDs occur earlier in the flash, especially for flashes with low multiplicities. −CIDs occur later in the lifetime of a flash, regardless of multiplicity. This measure of τ_{flash} and multiplicity is highly affected by event detection efficiency (Antunes de Sá et al., 2021), which might explain some of the variability.

A supercell that occurred on November 10 is particularly useful in validating the classification because it occurred in the middle of the main RELAMPAGO instrument deployment region. As an example of the EIC validation capability for this data set, Figure 6 shows the set of four LF sferics for an observed +CID, and an XLMA-style plot of CAMMA sources (LMA sources are also available). The sferic panel includes the classification features *A–D* explained in Section 3.1, as well as the skywave peak observations used in the source height estimate, explained in Section 3.2. Sferics from LF1, LF2, and LF3, all saturated to a certain extent, which certainly affected their waveform features, and so these were not used in the computation of the classification parameters. The identification of skywave peaks is also successful, yielding 3 pairs of observations for the ionosphere and source height estimates. Note that other observation pairs were erroneously identified (not shown) but subsequently discarded by the innovation filter. The XLMA-style plot shows the isolated CID (light-blue triangle) occurred between two flashes, with a coinciding CAMMA source within 2 km in altitude, within the uncertainty of both sources. The EICs in this storm are investigated in the next section.

5. Storm Case-Studies

5.1. November 10, 2018, 19:30–22:30 UTC

A severe storm with supercellular characteristics (Trapp et al., 2020) moved eastward during IOP4 through the RELAMPAGO domain between 19:30–22:30 UTC on November 10, 2018 and stayed within 100 km of LF2, with flashes occurring within a few kilometers of the station around 20:30 UTC and the LMA indicating a lightning hole. This supercell storm is one of the best RELAMPAGO examples for EIC research in terms of data availability. It displayed a relatively high number of CIDs, and was observed by most of the major RELAMPAGO instruments, including radar sites.

Figure 7 presents a map of the CID occurrence along with a time evolution panel during that storm. The two maps at the top of Figure 7 display the locations of identified EICs (left map), and locations of all LF flashes for this storm (right map), with markers color coded by UTC time. The location markers are overlaid on ABI band 3 data for 22:05 UTC. The time evolution panel, below the maps, contains four plots. From top to bottom, the first plot shows EIC and LF flash rates (#/minute), the second plot shows the distribution of flash peak current, and the third and fourth plots show a height distribution of all LMA sources in linear and log scales. Also on the third plot, +CID (red) and −CID (blue) source heights (circles) and coinciding LMA source heights (crosses) within 1 ms and 25 km are overlaid on the LMA height distribution. Before 20:40 UTC, only six LMA stations were operating, which is responsible for low detection efficiency, but a seventh station went online after that time providing higher quality data. Two animations are provided in the Supporting Information S1, highlighting this storm evolution and CID occurrence. In the LMA source density animation, Movie S2, a lightning hole is observed between 20:50 and 21:00 UTC.

Although the charge structure in this storm cannot be easily identified, given the low number of LMA stations, and might have been highly variable given its supercell characteristics, it is clear that the much higher +CID heights are occurring in the overshooting tops, possibly above a normal upper positive charge layer, or within a top negative layer of an inverted structure. The lower number of LMA operating stations prior to 20:40 UTC unfortunately prevents a conclusive understanding of the charge structure. A number of lower altitude −CIDs, and of even lower +CIDs, later in the storm might suggest a normal charge structure, consistent with the more common CID heights reported in the literature (e.g., Lyu et al., 2015; Smith et al., 2004; Wu et al., 2012; Zhang et al., 2016).

5.2. November 12, 2018, 13:00–15:30 UTC

In contrast to the November 10 severe storm, one of the nonsevere storms of November 12 is shown in Figure 8, a similar panel to Figure 7. This storm occurred between 13:00–15:30 UTC moving south from near the city of Río Cuarto. Even though the storms on this day were not severely convectional based on their lightning production and weaker in comparison to the storms that occurred on November 10, there was a high variability in +CID occurrence. The case shown here is the one with the highest percentage of +CID occurrence of all observed storms, comprising about 40% of all events with a peak current higher than 10 kA, and of the highest average peak current observed in the RELAMPAGO LF lightning data. Given the energy budget of these weak storms, the extraordinarily high-peak currents seen are likely due to the speed of the breakdown, while the charge transfer is actually relatively small (see Rison et al., 2016).

The more common CID height around 10 km is more prevalent in this storm as seen in Figure 8, and on most RELAMPAGO storms excluding the cases on November 10. Nonetheless, a population of higher altitude CIDs is still observed. Because of the large distance between this storm and the LMA, very few LMA sources are detected and they cannot provide validation of CID heights or charge layers.

Further studies are needed to understand where these high peak currents and high CID prevalence storms occur and what differentiates them from storms with less CID occurrence. Are they associated with higher IC prevalence storms, strong updrafts (Suszcynsky & Heavner, 2003), and/or geographical conditions (Ahmad et al., 2010; Sharma et al., 2008)?
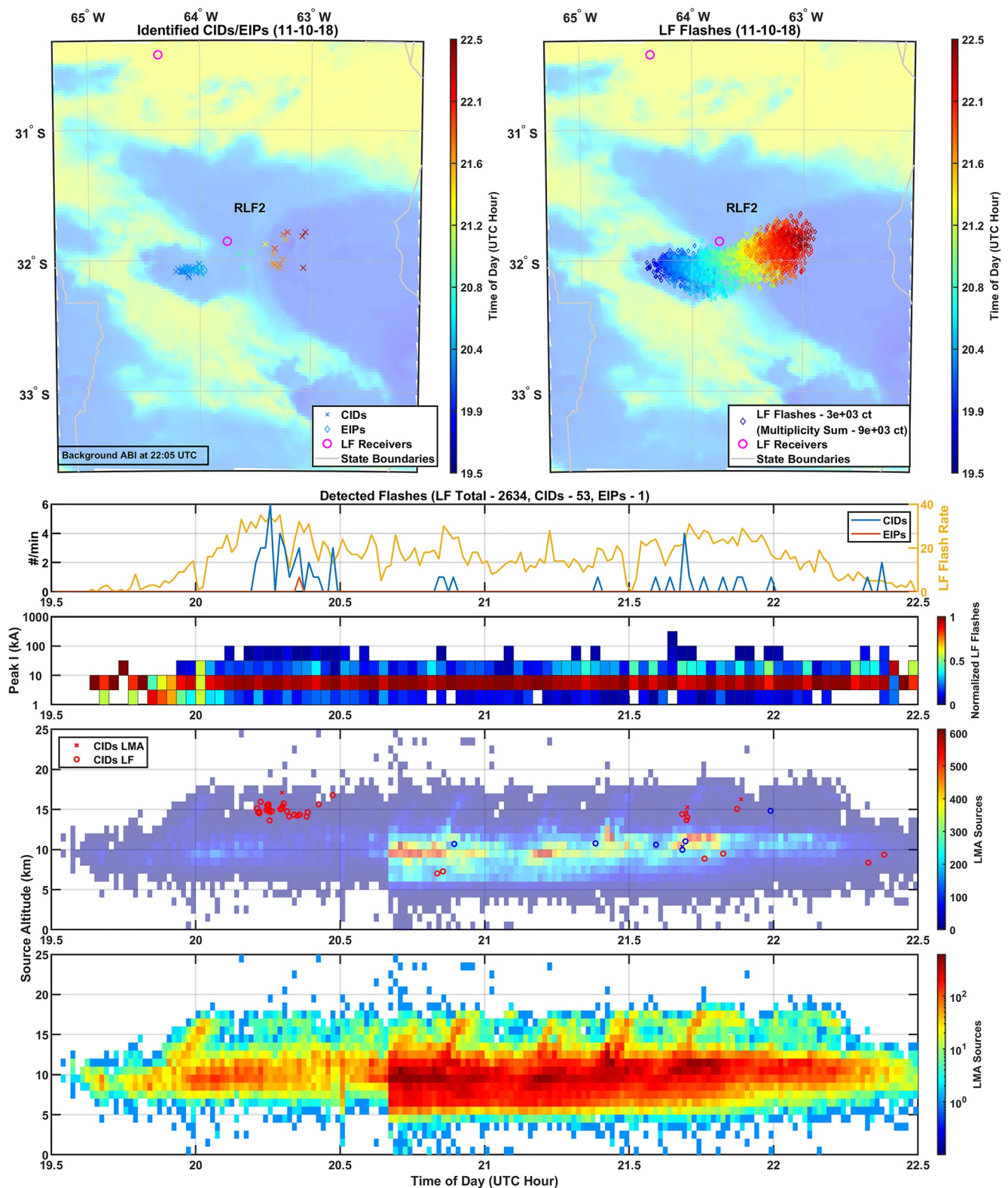
Figure 7. Energetic intracloud (EIC) panel displaying maps of the identified Compact Intracloud Discharges (CIDs) and Energetic In-cloud Pulses (EIP) (top left), and all LF flashes (top right) for the November 10, 2018, 19:30–22:30 UTC storm near LF2. Satellite imagery from ABI band 3 is shown in the background. The bottom panel presents the time evolution for EICs in this storm, including EIC rates, flash peak current distribution, +CID (red) and −CID (blue) source heights (circles), and coinciding LMA source heights (crosses) within 1 ms and 25 km on top of the distribution of all LMA source heights. The one EIP candidate identified here is actually a CG validated by CAMMA.
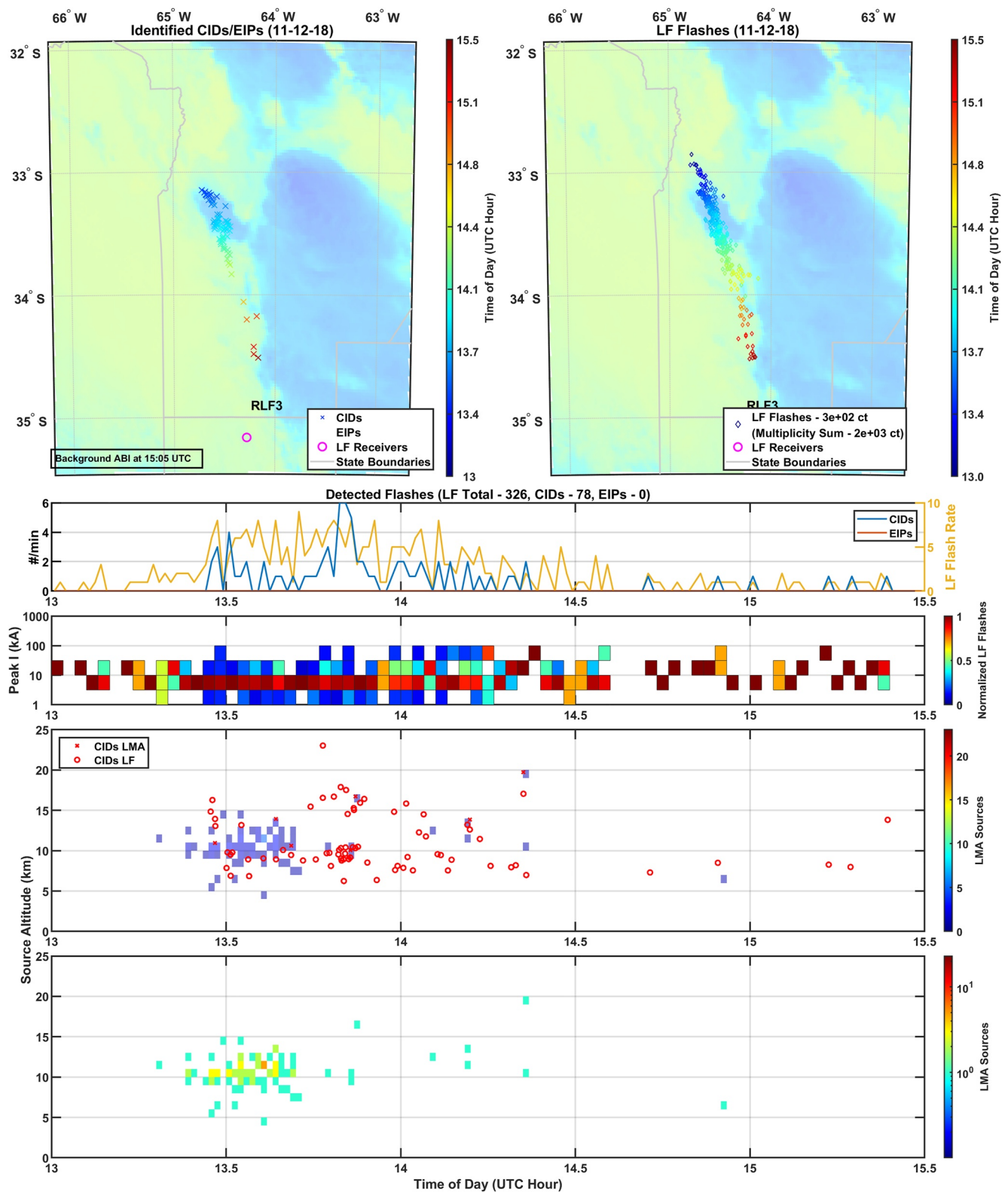
Figure 8. Energetic intracloud (EIC) panel displaying maps of the identified Compact Intracloud Discharges (CIDs) and Energetic In-cloud Pulse (top left) and all LF flashes (top right) for the November 12, 2018, 13:00–15:30 UTC Storm. Satellite imagery from ABI band 3 is shown in the background. The bottom panel presents the time evolution for EICs in this storm, including EIC rates, peak current distribution, +CID (red) and −CID (blue) source heights (circles) and coinciding LMA source heights (crosses) within 1 ms and 25 km, on top of the distribution of all LMA source heights.

6. Summary

In this study, we have investigated the classification of energetic intracloud lightning events during the RELAMPAGO campaign in Argentina in late 2018. The EIC classification implementation is described in the context of previously established research, with comprehensive details on the sferic feature identification. Similarly, an implementation of EIC height estimations using skywaves was built upon established literature, but additional implementation details were presented, particularly in prefit (innovation) editing. An EIC catalog was built for the entire RELAMPAGO LF data set, and validated, when possible, using other available data sets such as from LMA, CAMMA, or ENTLN. A small number of high peak current events that might not have been present in the LF Level 2 data were added by using ENTLN sources. The classification of CIDs proved to be straightforward due to the clearly distinct population of CIDs in the classification parameter space, with a low number of false positives (<3%). Most candidate EIPs, on the other hand, did not pass manual validation. Many suffered from misidentification of their sferics' main peak when the skywave merged with the groundwave for lightning sources far from the receiver. Saturation heavily distorted the high peak current sources eligible for EIP classification. Lastly, a low number of 200+ kA events, a loose requirement for EIP classification, did not provide enough samples for this study. Properties of RELAMPAGO CIDs, both positive and negative polarity, were investigated. Those properties largely agree with past research on CIDs. The most striking observation was that of higher altitude + CIDs than expected, for November 10, and high variability of CID prevalence, as high as 40% of 10+ kA events, in ordinary storms on November 12. The unusually high +CID populations on November 10 seemed to be associated with overshooting tops, but further investigation on charge structure and storm kinematics is needed.

Using the LF EIC data set produced and described in this paper, along with other meteorological data sets, future research can address CID variability and height in RELAMPAGO storms. In particular, future work should be aimed at understanding the extreme difference in CID occurrence between nonsevere storms on November 3 and 12, and further investigating the supercells on November 10 with high-altitude +CIDs and few −CIDs.

Data Availability Statement

RELAMPAGO LF, LMA, ABI, and GLM data sets used for this research are available in these in-text data citation references: (Deierling et al., 2019), (T. Lang, 2020), (GOES-R Calibration Working Group & GOES-R Program Office, 2017), and (GOES-R Series Program, 2019). ENTLN data supporting this research are available upon request from Earth Networks (Earth Networks, 2020).

References

Ahmad, N. A., Fernando, M., Baharudin, Z., Cooray, V., Ahmad, H., & Malek, Z. A. (2010). Characteristics of narrow bipolar pulses observed in Malaysia. *Journal of Atmospheric and Solar-Terrestrial Physics*, *72*(5–6), 534–540. https://doi.org/10.1016/j.jastp.2010.02.006

Antunes de Sá, A., Marshall, R., & Deierling, W. (2021). Lightning geolocation and flash rates from LF radio observations during the RELAMPAGO field campaign. *Earth and Space Science*, *8*, e2021EA001813. https://doi.org/10.1029/2021EA001813

Antunes de Sá, A., Marshall, R., Sousa, A., Viets, A., & Deierling, W. (2020). An array of low-cost, high-speed, autonomous electric field mills for thunderstorm research. *Earth and Space Science*, *7*(11), e2020EA001309. https://doi.org/10.1029/2020ea001309

Arabshahi, S., Dwyer, J. R., Nag, A., Rakov, V. A., & Rassoul, H. K. (2014). Numerical simulations of compact intracloud discharges as the relativistic runaway electron avalanche-extensive air shower process. *Journal of Geophysical Research: Space Physics*, *119*(1), 479–489. https://doi.org/10.1002/2013ja018974

Carey, L., Bitzer, P., & Medina, B. (2019a). *Cordoba Argentina marx meter array (camma) level 1 data*. version 1.0. UCAR/NCAR - Earth Observing Laboratory. https://doi.org/10.26023/EZ1X-DM4B-EN0V

Carey, L., Bitzer, P., & Medina, B. (2019b). *Cordoba Argentina marx meter array (camma) level 2 data*. version 1.1. UCAR/NCAR - Earth Observing Laboratory. https://doi.org/10.26023/VRN7-1FJY-0X01

Cecil, D. J., & Blankenship, C. B. (2012). Toward a global climatology of severe hailstorms as estimated by satellite passive microwave imagers. *Journal of Climate*, *25*(2), 687–703. https://doi.org/10.1175/jcli-d-11-00130.1

Cecil, D. J., Buechler, D. E., & Blakeslee, R. J. (2015). TRMM LIS climatology of thunderstorm occurrence and conditional lightning flash rates. *Journal of Climate*, *28*(16), 6536–6547. https://doi.org/10.1175/jcli-d-15-0124.1

Cohen, M. B., Inan, U., & Paschal, E. (2010). Sensitive broadband ELF/VLF radio reception with the AWESOME instrument. *IEEE Transactions on Geoscience and Remote Sensing*, *48*(1), 3–17. https://doi.org/10.1109/tgrs.2009.2028334

Cohen, M. B., Said, R., & Inan, U. (2010). Mitigation of 50–60 hz power line interference in geophysical data. *Radio Science*, *45*(6), 1–12. https://doi.org/10.1029/2010rs004420

Cummer, S. A., Lyons, W. A., & Stanley, M. A. (2013). Three years of lightning impulse charge moment change measurements in the United States. *Journal of Geophysical Research: Atmospheres*, *118*(11), 5176–5189. https://doi.org/10.1002/jgrd.50442

Deierling, W., Marshall, R., Sá, A., & Sousa, A. (2019). *Low frequency autonomous magnetic field sensors (lfams) level 1 data.* version 1.1. UCAR/NCAR - Earth Observing Laboratory. https://doi.org/10.26023/3CNH-AMVJ-B0D

Deierling, W., Marshall, R., Sá, A., & Sousa, A. (2021). *Low frequency autonomous magnetic field sensors (lfams) level 2 data.* version 1.0. UCAR/NCAR - Earth Observing Laboratory. https://doi.org/10.26023/3Z4Y-BY1N-ZM0W

Eack, K. B. (2004). Electrical characteristics of narrow bipolar events. *Geophysical Research Letters*, *31*(20), L20102. https://doi.org/10.1029/2004gl021117

Earth Networks. (2020). *Earth networks lightning network.* Retrieved from https://www.earthnetworks.com/why-us/networks/lightning/

Fishman, G. J., Bhat, P. N., Mallozzi, R., Horack, J. M., Koshut, T., Kouveliotou, C., et al. (1994). Discovery of intense gamma-ray flashes of atmospheric origin. *Science*, *264*(5163), 1313–1316. https://doi.org/10.1126/science.264.5163.1313

Franz, R. C., Nemzek, R. J., & Winckler, J. R. (1990). Television image of a large upward electrical discharge above a thunderstorm system. *Science*, *249*(4964), 48–51. https://doi.org/10.1126/science.249.4964.48

Fukunishi, H., Takahashi, Y., Kubota, M., Sakanoi, K., Inan, U. S., & Lyons, W. A. (1996). Elves: Lightning-induced transient luminous events in the lower ionosphere. *Geophysical Research Letters*, *23*(16), 2157–2160. https://doi.org/10.1029/96gl01979

GOES-R Calibration Working Group, & GOES-R Program Office (2017). *Noaa goes-r series advanced baseline imager (abi) level 1b radiances.* NOAA National Centers for Environmental Information. https://doi.org/10.7289/V5BV7DSR

GOES-R Series Program. (2019). *Noaa goes-r series geostationary lightning mapper (glm) level 0 data.* NOAA National Centers for Environmental Information. https://doi.org/10.25921/QC2R-PS67

Gurevich, A., Medvedev, Y., & Zybin, K. (2004). New type discharge generated in thunderclouds by joint action of runaway breakdown and extensive atmospheric shower. *Physics Letters A*, *329*(4–5), 348–361. https://doi.org/10.1016/j.physleta.2004.06.099

Gurevich, A. V., & Zybin, K. P. (2005). Runaway breakdown and the mysteries of lightning. *Physics Today*, *58*(5), 37–43. https://doi.org/10.1063/1.1995746

Heckman, S. (2014). Entln status update. In *Xv international conference on atmospheric electricity* (pp. 15–20).

Inan, U. S., Bell, T. F., & Rodriguez, J. V. (1991). Heating and ionization of the lower ionosphere by lightning. *Geophysical Research Letters*, *18*(4), 705–708. https://doi.org/10.1029/91gl00364

Inan, U. S., Cummer, S. A., & Marshall, R. A. (2010). A survey of ELF and VLF research on lightning-ionosphere interactions and causative discharges. *Journal of Geophysical Research*, *115*(A6), A00E36. https://doi.org/10.1029/2009ja014775

Lang, T. (2020). *Remote sensing of electrification, lightning, and mesoscale/microscale processes with adaptive ground observations (relampago) lightning mapper array (lma).* NASA Global Hydrology Resource Center DAAC. https://doi.org/10.5067/RELAMPAGO/LMA/DATA101

Lang, T. J., Ávila, E. E., Blakeslee, R. J., Burchfield, J., Wingo, M., Bitzer, P. M., et al. (2020). The RELAMPAGO lightning mapping array: Overview and initial comparison with the geostationary lightning mapper. *Journal of Atmospheric and Oceanic Technology*, *37*(8), 1457–1475. https://doi.org/10.1175/jtech-d-20-0005.1

Liu, N., Dwyer, J. R., & Cummer, S. A. (2017). Elves accompanying terrestrial gamma ray flashes. *Journal of Geophysical Research: Space Physics*, *122*(10), 10563–10576. https://doi.org/10.1002/2017ja024344

Liu, N., Dwyer, J. R., Tilles, J. N., Stanley, M. A., Krehbiel, P. R., Rison, W., & Wilson, J. G. (2019). Understanding the radio spectrum of thunderstorm narrow bipolar events. *Journal of Geophysical Research: Atmospheres*, *124*(17–18), 10134–10153. https://doi.org/10.1029/2019jd030439

Lyu, F., & Cummer, S. A. (2018). Energetic radio emissions and possible terrestrial gamma-ray flashes associated with downward propagating negative leaders. *Geophysical Research Letters*, *45*(19), 10764–10771. https://doi.org/10.1029/2018gl079424

Lyu, F., Cummer, S. A., Briggs, M., Marisaldi, M., Blakeslee, R. J., Bruning, E., et al. (2016). Ground detection of terrestrial gamma ray flashes from distant radio signals. *Geophysical Research Letters*, *43*(16), 8728–8734. https://doi.org/10.1002/2016gl070154

Lyu, F., Cummer, S. A., Krehbiel, P. R., Rison, W., Briggs, M. S., Cramer, E., & Stanbro, M. (2018). Very high frequency radio emissions associated with the production of terrestrial gamma-ray flashes. *Geophysical Research Letters*, *45*(4), 2097–2105. https://doi.org/10.1002/2018gl077102

Lyu, F., Cummer, S. A., & McTague, L. (2015). Insights into high peak current in-cloud lightning events during thunderstorms. *Geophysical Research Letters*, *42*(16), 6836–6843. https://doi.org/10.1002/2015gl065047

Marshall, R. A. (2012). An improved model of the lightning electromagnetic field interaction with the d-region ionosphere. *Journal of Geophysical Research*, *117*(A3), A03316. https://doi.org/10.1029/2011ja017408

Marshall, R. A., da Silva, C. L., & Pasko, V. P. (2015). Elve doublets and compact intracloud discharges. *Geophysical Research Letters*, *42*(14), 6112–6119. https://doi.org/10.1002/2015gl064862

Nag, A., & Rakov, V. A. (2010). Compact intracloud lightning discharges: 1. mechanism of electromagnetic radiation and modeling. *Journal of Geophysical Research*, *115*(D20), D20102. https://doi.org/10.1029/2010jd014235

Nesbitt, S. (2020). *Relampago-cacti.* Retrieved from https://sites.google.com/illinois.edu/relampago/home

Orville, R. E. (1991). Calibration of a magnetic direction finding network using measured triggered lightning return stroke peak currents. *Journal of Geophysical Research*, *96*(D9), 17135–17142. https://doi.org/10.1029/91jd00611

Rasmussen, K. L., Zuluaga, M. D., & Houze, R. A. (2014). Severe convection and lightning in subtropical South America. *Geophysical Research Letters*, *41*(20), 7359–7366. https://doi.org/10.1002/2014gl061767

Rison, W., Krehbiel, P. R., Stock, M. G., Edens, H. E., Shao, X.-M., Thomas, R. J., & Zhang, Y. (2016). Observations of narrow bipolar events reveal how lightning is initiated in thunderstorms. *Nature Communications*, *7*(1), 10721. https://doi.org/10.1038/ncomms10721

Rison, W., Thomas, R. J., Krehbiel, P. R., Hamlin, T., & Harlin, J. (1999). A GPS-based three-dimensional lightning mapping system: Initial observations in central New Mexico. *Geophysical Research Letters*, *26*(23), 3573–3576. https://doi.org/10.1029/1999gl010856

Sharma, S., Fernando, M., & Cooray, V. (2008). Narrow positive bipolar radiation from lightning observed in Sri Lanka. *Journal of Atmospheric and Solar-Terrestrial Physics*, *70*(10), 1251–1260. https://doi.org/10.1016/j.jastp.2008.03.002

Smith, D. A., Eack, K. B., Harlin, J., Heavner, M. J., Jacobson, A. R., Massey, R. S., & Wiens, K. C. (2002). The Los Alamos sferic array: A research tool for lightning investigations. *Journal of Geophysical Research*, *107*(D13). ACL 5-1-ACL 5-14. https://doi.org/10.1029/2001JD000502

Smith, D. A., Heavner, M. J., Jacobson, A. R., Shao, X. M., Massey, R. S., Sheldon, R. J., & Wiens, K. C. (2004). A method for determining intracloud lightning and ionospheric heights from VLF/LF electric field records. *Radio Science*, *39*(1), RS1010. https://doi.org/10.1029/2002rs002790

Smith, D. A., Shao, X. M., Holden, D. N., Rhodes, C. T., Brook, M., Krehbiel, P. R., et al. (1999). A distinct class of isolated intracloud lightning discharges and their associated radio emissions. *Journal of Geophysical Research*, *104*(D4), 4189–4212. https://doi.org/10.1029/1998jd200045

Suszcynsky, D. M., & Heavner, M. J. (2003). Narrow bipolar events as indicators of thunderstorm convective strength. *Geophysical Research Letters*, *30*(17), 1879. https://doi.org/10.1029/2003gl017834

Tilles, J. N., Krehbiel, P. R., Stanley, M. A., Rison, W., Liu, N., Lyu, F., et al. (2020). Radio interferometer observations of an energetic in-cloud pulse reveal large currents generated by relativistic discharges. *Journal of Geophysical Research: Atmospheres*, *125*(20), e2020JD032603. https://doi.org/10.1029/2020jd032603

Tilles, J. N., Liu, N., Stanley, M. A., Krehbiel, P. R., Rison, W., Stock, M. G., et al. (2019). Fast negative breakdown in thunderstorms. *Nature Communications*, *10*(1), 1648. https://doi.org/10.1038/s41467-019-09621-z

Trapp, R. J., Kosiba, K. A., Marquis, J. N., Kumjian, M. R., Nesbitt, S. W., Wurman, J., et al. (2020). Multiple-platform and multiple-doppler radar observations of a supercell thunderstorm in South America during RELAMPAGO. *Monthly Weather Review*, *148*(8), 3225–3241. https://doi.org/10.1175/mwr-d-20-0125.1

Vine, D. M. L. (1980). Sources of the strongest RF radiation from lightning. *Journal of Geophysical Research*, *85*(C7), 4091–4095. https://doi.org/10.1029/jc085ic07p04091

Watson, S. S., & Marshall, T. C. (2007). Current propagation model for a narrow bipolar pulse. *Geophysical Research Letters*, *34*(4), L04816. https://doi.org/10.1029/2006gl027426

Willett, J. C., Bailey, J. C., & Krider, E. P. (1989). A class of unusual lightning electric field waveforms with very strong high-frequency radiation. *Journal of Geophysical Research*, *94*(D13), 16255–16267. https://doi.org/10.1029/jd094id13p16255

Wu, T., Dong, W., Zhang, Y., Funaki, T., Yoshida, S., Morimoto, T., & Kawasaki, Z. (2012). Discharge height of lightning narrow bipolar events. *Journal of Geophysical Research*, *117*(D5), D05119. https://doi.org/10.1029/2011jd017054

Wu, T., Dong, W., Zhang, Y., & Wang, T. (2011). Comparison of positive and negative compact intracloud discharges. *Journal of Geophysical Research*, *116*(D3), D03111. https://doi.org/10.1029/2010jd015233

Zhang, H., Lu, G., Qie, X., Jiang, R., Fan, Y., Tian, Y., et al. (2016). Locating narrow bipolar events with single-station measurement of low-frequency magnetic fields. *Journal of Atmospheric and Solar-Terrestrial Physics*, *143–144*, 88–101. https://doi.org/10.1016/j.jastp.2016.03.009

Zhu, Y., Bitzer, P., Stewart, M., Podgorny, S., Corredor, D., Burchfield, J., et al. (2020). Huntsville Alabama marx meter array 2: Upgrade and capability. *Earth and Space Science*, *7*(4), e2020EA001111. https://doi.org/10.1029/2020ea001111

Zipser, E. J., Cecil, D. J., Liu, C., Nesbitt, S. W., & Yorty, D. P. (2006). Where are the most intense thunderstorms on Earth? *Bulletin of the American Meteorological Society*, *87*(8), 1057–1072. https://doi.org/10.1175/bams-87-8-1057